Radiometric Estimation of Tropospheric Attenuation: a Mixed Physically-Based/Machine Learning Approach

Tuna Tunçkol, Marianna Biscarini, *Senior Member, IEEE*, Lorenzo Luini, *Senior Member, IEEE*

***Abstract* – A mixed physically based/machine learning approach to measure tropospheric attenuation *A* in all-weather conditions by means of microwave radiometers (MWRs) is proposed. The key idea is to combine the advantages originating from the accurate radiometric *A* retrievals, provided by the well-established Cosmic Background (CB) approach in clear-sky conditions, with the benefits coming from machine learning techniques. The latter aims at estimating *A* in rainy situations through a simplified approach able to overcome the issues posed by more complex techniques such as the standard solution of the Radiative Transfer Equation or the Sun Tracking (ST) microwave technique. To this aim, an artificial neural network is devised to turn the antenna noise temperatures measured by a 4-channel MWR (from Ka- to W-band) into tropospheric attenuation at the frequencies of the radiometric channels, namely 23.8, 31.4, 72.5 and 82.5 GHz. The network is properly trained and tested by taking advantage of the concurrent CB and ST measurements collected by the RpG radiometer deployed at Politecnico di Milano, Italy, under the ESA funded WRAD project. The proposed approach to retrieve the tropospheric attenuation is intended to overcome the limits associated both to the ST technique (only measurements during the day, link elevation strictly bound to the Sun ecliptic) and to the CB one (unreliable measurements in rainy conditions).**

***Index Terms* — Atmospheric attenuation, rain attenuation, radiometry, artificial neural network, satellite communications, mean radiating temperature.**

I. Introduction

Since the launch of the first communication-oriented commercial satellite in 1964 (Syncom 3), Earth-space communication systems have been characterized by a continuous increase in the carrier frequency, induced by the request of faster data rate (which implies wider bandwidths), by the technology advancement of microwave components and by the congestion of lower bands. The employment of Q/V bands in High Throughput Satellites (HTS) systems is rapidly taking place, and the utilization of the W band (75-110 GHz) emerges as the following step [1]. However, the higher the carrier frequency, the more detrimental is the influence of the troposphere on electromagnetic waves: wave phase delay, signal group delay, wave depolarization, signal attenuation (as a result of absorption and scattering), ray bending, signal scintillation and atmospheric noise contribution are some of the effects that cause the degradation of the link quality and the decrease in the link availability. Among them, attenuation certainly plays the most relevant role [2].

Designing Earth-space communication links at W band currently represents a challenge. On the one side, the availability of W-band propagation data is limited to terrestrial links, with the sole exception of the LEO-based experimental activity carried out in the framework of the ESA project "CubeSat-based W-band Channel Measurements" [3]. On the other side, the existing propagation models (e.g. those included in [4]) were mostly developed and tested based on the data gathered from experimental activities at frequencies up to the V band: the maximum frequency of the measurements collected from GEO (geostationary Earth orbit) satellites is 49.5 GHz (Italsat experiment). As a matter of fact, the accurateness of propagation models for the system design at W band remains an open question, which cannot be currently answered: there is a clear need for propagation measurements beyond 50 GHz.

This goal can be achieved through different kinds of experimental campaigns. The utilization of space-borne beacon signals offers an optimum option: the Alphasat Aldo Paraboni Experiment is the most recent (and currently ongoing) example of how long-term (Ka-band and Q-band) propagation data can be concurrently collected in several sites [5]. However, besides the current lack of W-band payloads onboard geostationary satellites (ideal orbit to guarantee the measurement continuity), this kind of experiments are complex and extremely expensive. More in general, space-borne signals, also those emitted by commercial satellites at Ku band and Ka band, can be used to collect data on the precipitation along the link [6], which can be in turn used to derive attenuation at higher frequencies.

A simpler and cheaper alternative is offered by ground-based microwave radiometers (MWR), which can be employed to characterize the tropospheric channel by taking advantage of retrieval algorithms receiving as input the measured sky noise data. The most common MWR operation mode consists in pointing the instrument at zenith or toward a satellite to collect brightness temperature data, which are converted into tropospheric attenuation by means of a simple inversion algorithm. This technique, referred to as "Cosmic background" (CB) operation mode for convenience of this paper, typically offers accurate results [7],[8], but its applicability is limited to cases when scattering can be neglected: in rainy conditions,

Tuna Tunçkol and Lorenzo Luini are with the Dipartimento di Elettronica, Informazione e Bioingegneria, Politecnico di Milano, Piazza Leonardo da Vinci, 32, 20133, Milano, Italy, via Ponzio 34/5, Milano 20133, Italy (e-mail: lorenzo.luini@polimi.it, tuna.tunckol@mail.polimi.it).

M. Biscarini is with the Department of Information Engineering, Electronics and Telecommunications (DIET), Sapienza University of Rome, 00184 Rome, Italy, (e-mail: marianna.biscarini@uniroma1.it).

radiometric retrievals of the tropospheric attenuation can significantly deviate from the reference beacon-derived data [9]. Indeed, at Ka-band and above, although there is still a significant impact of absorption and emission under rainy conditions, scattering effects must be considered too [10],[11]. A recently developed more complex technique, commonly referred to as "Sun tracking" (ST) operation, consists in alternatively switching the MWR antenna azimuth angle from towards the Sun to off the Sun (for a fixed elevation angle) while gradually changing the elevation angle to track the diurnal Sun trajectory [12],[13]. The utilization of the Sun as a sort of equivalent beacon emitter offers the possibility to retrieve the tropospheric attenuation in all-weather conditions, including rainy ones. Unfortunately, accurate ST measurements can present a challenge: pointing precisely at the Sun, which can be assimilated to a transmitter circular antenna whose half-power beamwidth is approximately 0.5°, might not be an easy task. This is even more challenging at W band, due to the reduction in the antenna beamwidth [14]. In addition, ST measurements are obviously available only during the day.

This contribution proposes a novel machine learning (ML) based approach to collect data of tropospheric attenuation *A* in all-weather conditions by exploiting MWRs. ML and neural networks techniques are in rapid expansion in basically every scientific area. In the remote sensing field, the first approaches were developed for image processing, classification, prediction and geophysical retrieval in general, with an increase in the last decades of techniques for the estimation of rainfall exploiting satellite passive observations [15],[16],[17]. In [18] an attempt to design a model-based neural-network approach for the estimation of the atmospheric extinction exploiting ground-based observations is proposed, where radiometric observations are completed with a specific rainfall radiative model in order to overcame the limitations of classical radiometric observations in rainy conditions. In [19], the authors propose a ML technique for the brightness temperature estimation with the limitation of assuming a constant value of the mean radiating temperature (which is the core quantity for the retrieval of the atmospheric attenuation through ground-based microwave radiometric measurements). To the authors' knowledge, currently there are no works devoted to the retrieval of the atmospheric mean radiating temperature through a ML approach, which is what is proposed in this work. Specifically, in this paper, an artificial neural network (ANN) is devised and used to convert the brightness temperatures measured by a 4-channel MWR into tropospheric attenuation at the frequencies of the radiometric channels, namely 23.8 GHz, 31.4 GHz, 72.5 GHz and 82.5 GHz. The network is properly trained and tested by taking advantage of the concurrent CB and ST measurements collected by the RpG radiometer deployed at Politecnico di Milano, Italy, in the framework of the ESA-funded project "WRAD - Characterization of W-band propagation channel through ground-based observations" [20]. This approach is intended to overcome the limits associated both to the ST technique (only measurements during the day, link elevation strictly bound to the Sun ecliptic) and to the CB one (unreliable measurements in rainy conditions).

This contribution is organized as follows: Section II recalls the main concepts underpinning the estimation of the tropospheric attenuation from radiometric measurements, while Section III illustrates the experimental setup and the propagation data. Section IV focuses on the machine learning based prediction technique, whose results and accuracy are discussed in Section V. Finally, Section VI presents some conclusions and offers some cues on the future work.

II. MWR Based Retrieval of the Tropospheric Attenuation

Microwave radiometers are passive instruments measuring the natural electromagnetic emission from tropospheric constituents, from which the associated attenuation can be retrieved by exploiting the radiative transfer equation (RTE) mathematical framework [21].

This goal can be mainly achieved by means of two measurement techniques briefly recalled in this section: the cosmic background technique and the Sun tracking technique.

A. Cosmic Background Technique

The interaction of the electromagnetic radiation with atmospheric constituents is duly mathematically described by the RTE, which takes into account the electromagnetic absorption, emission and scattering properties of the atmosphere. The Rayleigh-Jeans approximation of Planck's law, suitable for microwave frequencies, states that the electromagnetic emission of a blackbody, typically quantified in terms of brightness, is linearly dependent on its physical temperature. Thus, according to the RTE and adopting the Rayleigh-Jeans approximation, the overall sky thermal emission of a real body is referred to as brightness temperature T_B. If the considered real body is the Earth's atmosphere (i.e., the atmospheric constituents), the atmospheric brightness temperature for a ground observation, that means considering the downwelling atmospheric radiation, is given by [21]:

$$T_B(r) = T_B(0)\mathrm{e}^{-\tau(0,r)} + \int_0^{\mathrm{r}} k_e(r')[(1-a)T(r') + aT_{SC}(r')]\mathrm{e}^{-\tau(r',r)}\mathrm{d}r' \quad \mathrm{(K)} \qquad (1)$$

where $\vec{r} = r\vec{s}_0$ denotes the propagation direction within the Earth atmosphere, being $\vec{s}_0$ the unit vector indicating the observation direction. In (1), $T_B(r)$ is the brightness temperature observed at the point r (where we assume that the ground receiving antenna is positioned), which consists of the contribution of an atmospheric layer starting at level 0 (that, in our case, is the top of the atmosphere): $T(r')$ is the physical temperature at the generic intermediate point r', $T_B(0)$ is the brightness temperature at the boundary layer (i.e., the cosmic background temperature impinging on the top of the atmosphere T_C = 2.73 K), k_s is the scattering coefficient, k_e is the extinction coefficient, $a = k_s/k_e$ is the scattering albedo, τ is the optical thickness, and, finally, $T_{SC}(r)$ is the multiple scattering contribution. The latter is given by the radiation temperature coming from all the directions different from the considered propagation direction (i.e., scattered from the surrounding atmospheric particles), incident on the atmospheric particles located along the considered propagation direction and scattered toward the observation direction.

Equation (1) can be written in a simplified form introducing the sky mean radiating temperature T_{mr} (defined as the

temperature of the equivalent homogeneous isothermal atmospheric layer):

$$T_B(\theta,\varphi) = T_C \mathrm{e}^{-\tau(\theta,\varphi)} + T_{mr}\left[1 - \mathrm{e}^{-\tau(\theta,\varphi)}\right] \text{ (K)} \quad (2)$$

where the propagation direction is expressed through the antenna azimuth φ and elevation θ angles.

Recalling that the atmospheric attenuation is $A(\theta,\varphi) = -10\log_{10}\left[\mathrm{e}^{-\tau(\theta,\varphi)}\right]$ and by defining the antenna noise temperature T_A as the convolution between brightness temperature impinging on the antenna and the antenna directivity $D(\theta,\varphi)$,

$$T_A(\theta,\varphi) = \frac{1}{4\pi}\int_{4\pi} T_B(\theta,\varphi) D(\theta,\varphi) d\Omega \text{ (K)} \quad (3),$$

it follows that

$$A(\theta,\varphi) = 10\log_{10}\left(\frac{T_{mr} - T_C}{T_{mr} - T_A(\theta,\varphi)}\right) \text{ (dB)} \quad (4)$$

As a result, equation (4) allows retrieving A, the attenuation along the path in dB, from the measured antenna noise temperature and the cosmic background temperature (hence, the technique name), and provided that an estimate of T_{mr} is available. In scattering free conditions, T_{mr} can be quite accurately estimated from surface meteorological data [22], while in rainy ones, i.e. when k_s in (1) cannot be neglected, usual estimates of T_{mr} are not sufficiently accurate [23]: indeed, this is the main weakness to the use of the CB technique. Such limitation can be overcome when a radiometer and a beacon receiver are pointed along the same path, which allows deriving an accurate estimate of T_{mr} as illustrated e.g. in [24] and [25]. In the absence of a beacon receiver, different methodologies have been investigated in the past to estimate T_{mr} under scattering free conditions from surface meteorological data. In this work, we take advantage of the model described in the Appendix: T_{mr} is estimated from the surface temperature T_S (K) and the surface relative humidity RH_S (%), while taking in due account the dependence of T_{mr} on the elevation angle [8].

The main issue for the CB methodology is that, using T_{mr} as obtained from (5) under rainy conditions, $T_A(\theta,\varphi)$ is likely to exceed T_{mr}, which makes unusable the outputs of (4) [12].

B. Sun Tracking Technique

The idea underpinning the ST technique is to exploit the Sun as an equivalent space-borne electromagnetic radiator. In this case, two consecutive measurements are carried out by fixing the elevation angle θ_0 while switching the azimuth angle from φ_0 to φ_1 to alternatively point the instrument toward-the-Sun (twS) and off-the-Sun (ooS), respectively. In the former case, the brightness temperature measured by the MWR consists of the contribution coming from the Sun, attenuated by the atmosphere, as well as by the contribution of the atmospheric emission itself. In the latter case, the measurement is not affected by the Sun radiation, but only by the atmospheric emission [12],[13].

The comprehensive mathematical framework of the ST technique is described in [12] and [13], in which the reader can find additional details; here, it suffices to focus on the key concepts. As previously stated, the ST technique foresees to alternatively switch the MWR antenna pointing from towards the Sun to off the Sun at a given elevation angle. This is continuously repeated as the elevation angle changes to track the Sun diurnal trajectory. Using this approach, the tropospheric attenuation A_{ST} can be estimated as [12],[13]:

$$A_{ST}(\theta_0,\varphi_0) \cong 4.343 \ln\left[\frac{T^*_{Bsun}(\theta_0,\varphi_0)}{\Delta T_A(\theta_0,\varphi_0)}\right] \text{ (dB)} \quad (5)$$

where

$$\Delta T_A(\theta_0,\varphi_0) = T_{A-twS}(\theta_0,\varphi_0) - T_{A-ooS}(\theta_0,\varphi_1) \text{ (K)} \quad (6)$$

$T_{A-twS}(\theta_0,\varphi_0)$ and $T_{A-ooS}(\theta_0,\varphi_1)$ are the antenna noise temperatures measured when pointing towards and off the Sun, respectively. $T^*_{Bsun}(\theta_0,\varphi_0)$ is the Sun brightness temperature multiplied by the beam-filling factor (f_Ω), i.e. the ratio between the Sun radiation solid angle (Ω_{Psun}) and the antenna beamwidth radiation solid angle (Ω_{Pant}), $f_\Omega = \Omega_{Psun}/\Omega_{Pant}$. The latter can be affected by how precisely the antenna can track the Sun [12],[13],[14]. For A_{ST} to be an accurate estimate of the tropospheric attenuation, changing between ooS and twS observations needs to be fast enough to assume the atmospheric homogeneity (i.e. same optical thickness and mean radiative temperature between two consecutive observations). This implies choosing φ_1 large enough to prevent the Sun from intersecting the field of view of the radiometer antenna. Note that (6) requires to first evaluate the Sun brightness temperature, to be performed in clear sky conditions, as detailed in [12].

The ST technique permits to circumvent the issue of estimating T_{mr} by providing an attenuation retrieval method that is reliable in all-weather conditions, though also such a technique presents some limitation. In fact, under severe rainy conditions, the contribution of the Sun becomes negligible due to the strong attenuation by rain particles. In this case, ΔT_A in (7) may reach zero or even negative values, depending on the radiometer noise and the atmospheric variability between φ_0 and φ_1. This poses an upper limit to the application of the ST technique for the retrieval of tropospheric attenuation under rainy conditions [12].

III. Experimental Setup and Data Collection

The radiometric data were collected in the framework of the WRAD project funded by the European Space Agency, which kicked off in 2019 with the objective of performing a W-band ST measurements campaign [20] (45.48° N, 9.23° E). The ST-MWR, deployed at Politecnico di Milan, features two channels at 23.8 and 31.4 GHz (Ka-band) and two channels at 72.5 and 82.5 GHz (W-band). The instrument is equipped with a hydrophobic radome and a blower, both of which contribute to significantly reducing the possible accumulation of water on the radome surface, which, in turn, might contaminate the measurements. The device was built by RPG Physics GmbH and takes advantage of azimuth and elevation positioners (0.05° and 0.1° scan step, respectively) to enable different measurement modes, namely: Sun Tracking, Cosmic Background and File Tracking (FTK). The latter mode is conceived for a custom operation of the instrument: the user can specify in an FTK file the daily time series of the elevation and azimuth angles that the positioners will set. Fig. 1 shows the architecture for the automated operation of the instrument:

the Office PC produces the daily FTK files, executes the measurements schedule and communicates with the Host PC, which runs the RPG software (SW) to control the radiometer. The measured data are stored on the Host PC and can be easily retrieved by the Office PC for post processing.

The WRAD dataset is nominally available from October 2019 to August 2021, but the accuracy of the antenna pointing system was optimized only at the end of October 2020. In addition, around mid-January 2021 the noise diode of the W-band channels failed, which further limited the collection of W-band data. Table I reports the actual period of Ka- and W-band data availability between 2019 and 2021; two partially overlapping periods are defined: 'Period 1' (for the W-band channel availability) and 'Period 2' (for the Ka-band channel availability). Though the availability of W-band data is limited to approximately 2.5 months, these measurements definitely represent a valuable dataset, given the overall scarcity of such kind of data worldwide.

A weather station is installed at approximately 20 meters from the MWR to monitor the surface pressure *P*, the relative humidity *RH* and temperature *T*. At the same distance, a disdrometer is installed to measure the rain rate *RR*.

TABLE I. AVAILABILITY FOR THE MILANO ST MWR MEASUREMENTS.

Band	Availability period
W	01/11/2020 – 15/01/2021 (Period 1)
Ka	01/11/2020 – 08/08/2021 (Period 2)

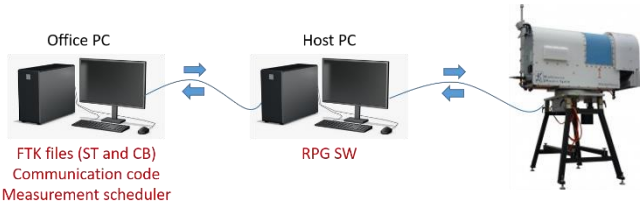

Fig. 1. Setup for automated radiometric measurements.

Fig. 2 shows a sample of the data measured by the MWR during a clear sky day, at 72.5 GHz. The top left-hand corner graph depicts the trend of the equivalent noise temperature: $T_{A\text{-}ooS}$ is maximum at low values of the Sun elevation (shown in the top right-end corner graph) because of the longer tropospheric path, i.e. an increased sky noise contribution. On the contrary, $T_{A\text{-}twS}$ is maximum in correspondence of the Sun elevation peak because the Sun radiation is less attenuated by the atmosphere, if compared to low elevations. Fig. 2 also shows that the path attenuation estimated using the ST mode is in very good agreement with the one estimated using the CB mode (bottom graph), which is the reference for atmospheric attenuation in absence of precipitations [7].

Further results are shown in Fig. 3, which reports the measurements collected during a rain event (see the bottom left-hand graph depicting *RR*): as expected, there is a marked discrepancy between the CB mode and ST mode attenuations, the latter being the reference method under rainy conditions (because of the impact of atmospheric particle scattering on the CB method) [12].

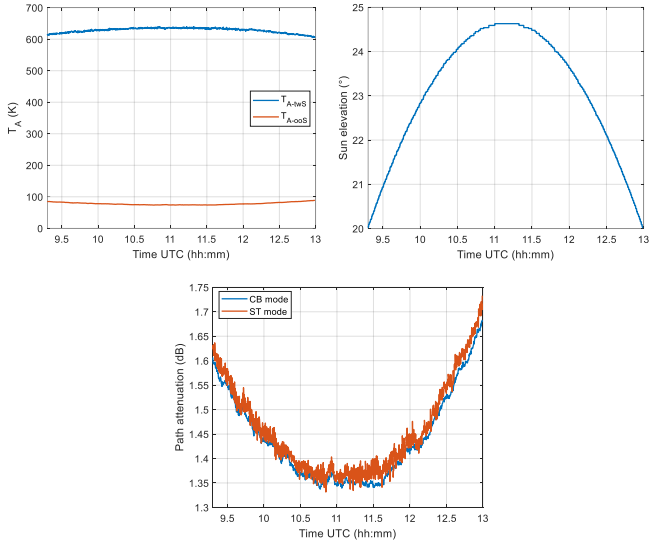

Fig. 2. Sample of the data measured by the ST-MWR during a clear sky day, at 72.5 GHz. From the top-left corner, in clockwise direction: T_A, Sun elevation and path attenuation.

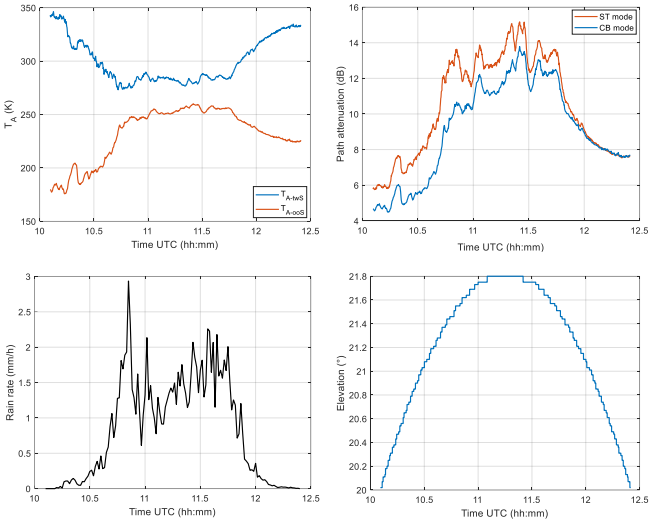

Fig. 3. Sample of the data measured by the ST-MWR during a rainy day, at 72.5 GHz. From the top-left corner, in clockwise direction: T_A , path attenuation, rain rate and Sun elevation.

IV. NEURAL NETWORK BASED APPROACH

The results in Fig. 3 show that the attenuation difference between the ST and the CB techniques reaches a peak of 3.5 dB, which gives a hint of how unreliable the latter approach can be under rainy conditions. On the other hand, accurate ST measurements are challenging: pointing precisely at the Sun might not be an easy task, even more so at W band, due to the reduction in the antenna beamwidth [14]. In addition, ST measurements cannot be collected at night time.

This Section proposes a new approach aimed at estimating the tropospheric attenuation from radiometric measurements: the objective is to preserve the advantages offered by the ST technique (application in all-weather conditions and high accuracy), while circumventing the associated challenges, i.e. precise Sun pointing and collection of the data only during the day. This goal can be achieved by resorting to an artificial neural network, receiving as input T_A measurements collected

using the CB approach (as well as meteorological ones) and providing as output an estimate of the mean radiating temperature T_{mr}. From the knowledge of the latter, the tropospheric attenuation A can be calculated using (4). As described in detail in the subsections below, the network training will take advantage of the concurrent ST and CB measurements collected during the WRAD campaign.

A. Data Preparation

The power of ANNs lies in the fact of providing a simple tool to model the relationship between given inputs and outputs, which is especially useful if such a relationship is mathematically complex and/or no closed-form solution exists. This is the case of the radiative transfer equation in scattering conditions.

Fig. 4 depicts the inputs and outputs of the proposed ANN: the network is fed with the information provided by the weather sensors and with the off the Sun radiometric measurements, $T_{A\text{-}ooS}$, which de facto correspond to CB measurements. Although the rain rate measured at one point is not fully representative of the precipitation along the whole (slant) path, it is still expected to be a paramount input parameter. The network output is the mean radiating temperature T_{mr}, which is a key parameter driving the prediction of the tropospheric attenuation through (4) [26]. It is worth pointing out that $T_{A\text{-}ooS}$ in Fig. 4 includes all the available radiometric measurements, while T_{mr} is estimated for a specific frequency channel: though the network structure will not change, a different set of coefficients will be derived for each of the four frequencies. A further note is necessary on this point for the sake of clarity: as the data availability periods in Table I are different for the two bands, for Period 1, four channels were used as input to the network, while for Period 2, only the Ka-band ones were employed (as no W-band data are available in that period).

The target values of T_{mr}, necessary to train the ANN, are derived from the peculiar WRAD dataset. Specifically, equation (4) is inverted as follows:

$$T_{mr} = \frac{kT_{A-ooS}(\theta_0,\varphi_1)-T_C}{1-k} \text{ (K)} \quad (7)$$

$$k = 10^{\frac{A_{ST}(\theta_0,\varphi_0)}{10}}.$$

Fig. 4. Inputs and outputs of the proposed ANN.

When training an ANN, it is often required to scale the input data to improve the network accuracy, especially if the range of variation of the input features is strongly different, which is the case for the ANN reported in Fig. 4. The most common scaling techniques are normalization and standardization [27],[28], the latter being considered in this work. Standardization consists in scaling the original input feature X into a new variable X_n whose mean value is 0 and whose standard deviation is 1:

$$X_n = \frac{X-\mu}{\sigma} \quad (8)$$

where μ and σ are the mean and standard deviation values of X, respectively.

In addition, the logarithmic transformation is applied to the target data Y to obtain the new variable Y_n that has a more skewed distribution of the output, which, in turn, contributes to increasing the network accuracy [29]:

$$Y_n = \log(Y) \quad (9)$$

Another key step in the design of an ANN is to divide the available dataset into different subsets, each one used for a different purpose: training, validation and test [30]. The first set of data is used to train the model, i.e. to derive the coefficients that map at best the inputs to the outputs. The test dataset contains samples that are not used for training, so they can be employed to assess independently the accuracy of the outputs provided by the network. Finally, the validation data are used to avoid overfitting, i.e. that the network offers an extremely high accuracy only when using the training dataset, and consequently a poor performance on any other additional data. It is common to initially isolate 10% -20% of total data for test, the remaining part being employed for training. Afterwards, a further split could be applied (25%) to training data to extract the validation dataset. In this work, approximately 10% of Ka-band data and 15% of W-band data are reserved for testing. The remaining data (90% and 85% for Ka band and W band, respectively) then are split into 75% for training and 25% for validation. With the aim of maximizing the effectiveness of the ANNs, the available data were selected for training/validation or test based on the rationale of maintaining the same balance between rainy days and clear-sky days in each of the datasets: in fact, the dynamics of the tropospheric attenuation under rainy conditions is expected to be much higher (i.e. the estimation more difficult) than during clear sky days. Specifically, Table II lists the clear-sky and rainy days selected to test the ANNs, while the remaining ones were employed for the training/validation phase.

TABLE II. CLEAR-SKY AND RAINY DAYS SELECTED TO TEST THE ANNS.

Frequency (GHz)	Rain free days	Rainy days
23.84	4 and 28 Nov 2020 25 Jan 2021 21 Feb 2021 10 Mar 2021 5 and 17 Apr 2021 10 and 25 Jun 2021 10 and 19 Jul 2021 6 Aug 2021	9-20 Dec 2020 2-21 Jan 2021 3 Feb 2021
31.4	7-29 Nov 2020 16 Dec 2020 28 Jan 2021 1-14 Feb 2021 14-21 Mar 2021 18 May 2021 1-28 Jun 2021 8 Aug 2021	1-8-20 Dec 2020 4 Jan 2021 11 Apr 2021
72.5	5-24-29 Nov 2020 16 Dec 2020 8 Jan 2021	9-20-24 Dec 2020 2 Jan 2021
82.5	10-29 Nov 2020 17-31 Dec 2020 7 Jan 2021	8-20-24 Dec 2020 2 Jan 2021

The identification of rainy days was achieved by relying both on the collocated weather sensors (mainly the rain rate)

and on the visually inspection of the data. In fact, the disdrometer provides point measurements of the precipitation, which is not always representative of the signature of rain on the signal along the slant path.

B. Model Development

The ANN development was achieved by taking advantage of Matlab Deep Learning Toolbox. Specifically, the "fitrnet" function was used to train the network [31]. This function trains ANNs with the fully connected feed-forward multilayer perceptron (MLP) architecture, using the Limited Memory Braydon Fletcher Goldfarb Shannon (L-BFGS) optimization algorithm. The function optionally applies the input data standardization. The overall implementation of the network is summarized in Fig. 5.

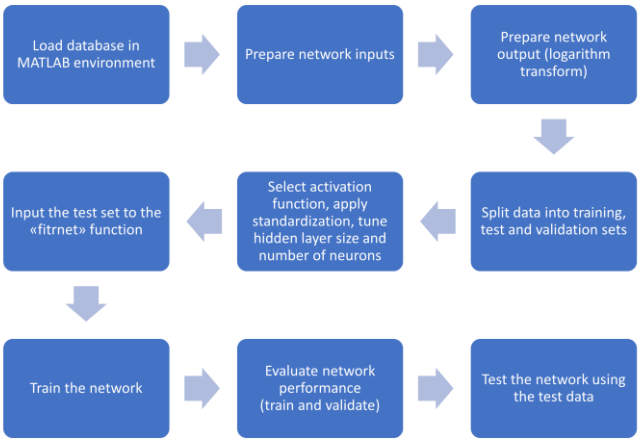

Fig. 5. Flowchart summary of the network training and test.

A different network model is obtained for each frequency channel: the details of each network are summarized in Table III. The number of hidden layers and neurons are determined by following the straightforward "trial-and-error" approach: the network complexity was gradually increased until no further significant improvements in the accuracy were achieved, as further detailed in the next Section. Regarding the neuron activation function, the rectified linear unit (reLU) was chosen.

TABLE III. DETAILS ON THE ANNS.

Frequency (GHz)	Number of hidden layers	Number of neurons
23.84	3	[11,8,5]
31.40	3	[11,8,5]
72.50	2	[12,7]
82.50	2	[15,6]

The selection of the number of hidden layers and neurons is typically the result of a compromise. On the one hand, a small amount of hidden layers and neurons will yield a limited accuracy, as the ANN will not be able to properly represent the complex relationship between the input and the output data. On the other hand, large network architectures could result in a high computational burden (and sometimes overfitting), especially while working with large datasets. In this regard, the difference in the number of hidden layers indicated in Table III might depend on the type of events predicted at the different frequencies. W-band data are only available for late Autumn and early Winter (Period 1), both characterized only by stratiform events (slow variations in time and limited rain intensity). On the other hand, Ka-band data cover a longer period (Period 2) including different seasons, i.e. both stratiform and convective events (quick variation in time and high rain intensity). As the networks associated to Ka-band channels allows predicting T_{mr} under diversified rainy conditions (stratiform and convective), their complexity can be expected to be higher than the one associated to W-band networks.

The performance of the network can be quantified by inspecting the loss scores after each training, all expressed in terms of mean squared error (MSE). It is common practice to consider two types of loss scores: training and validation. The former is a more general indicator of the network accuracy: it is calculated on the testing dataset and it is used to iteratively update the network parameters (weights and biases). The latter is calculated on the validation dataset to point out a possible overfitting: this occurs when the two loss scores diverge at some point of the training process. Fig. 6 offers a typical example of the convergence of the abovementioned losses for a successful network training (f = 31.40 GHz).

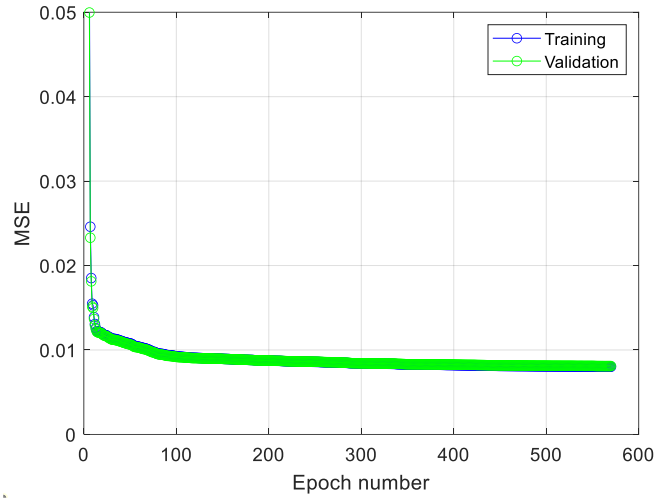

Fig. 6. Convergence of the training and validation losses for a successful network training (f = 31.40 GHz).

The overall training results for each network are listed in Table IV.

TABLE IV. TRAINING RESULTS FOR EACH NETWORK.

Frequency (GHz)	MSE	Training time (s)
23.84 GHz	0.0076	10.7
31.40 GHz	0.0079	22.67
72.50 GHz	0.00041	0.675
82.50 GHz	0.00094	2.3

V. RESULTS AND DISCUSSION

A. Daily Basis Analysis

The ANN performance can be assessed either by looking at the prediction of T_{mr}, or, more informatively, directly in terms of the tropospheric attenuation A. Fig. 7 compares A for a clear-sky day (28 November 2020), as obtained by means of the ST (A_{ST}) and CB (A_{CB}) techniques (red and yellow solid lines, respectively) and as estimated using the ANN (A_{NN}, blue solid

line). In this case, all curves are in agreement: the CB technique is accurate in conditions with no scatter, the ST technique offers a good accuracy in all-weather conditions and the ANN provides a precise prediction as well. A more critical comparison is offered for two rainy days in Fig. 8 (8 December 2020, light rain) and Fig. 9 (2 January 2021, moderate rain): as expected, the attenuation obtained from the ANN approach better agrees with the reference ST-based estimation, if compared to one derived from the application of the CB framework. The discrepancy increases with frequency, due to the associated enhancement of the tropospheric effects moving from Ka band to W band. Fig. 9 clearly points out that the attenuation estimated through the CB approach reaches higher values as the precipitation intensity increases, thus leading to strong inaccuracies and, in most cases, to the overestimation of A (see Fig. 10): this is due to the inaccuracy of T_{mr} estimations obtained from surface parameters, under rain conditions.

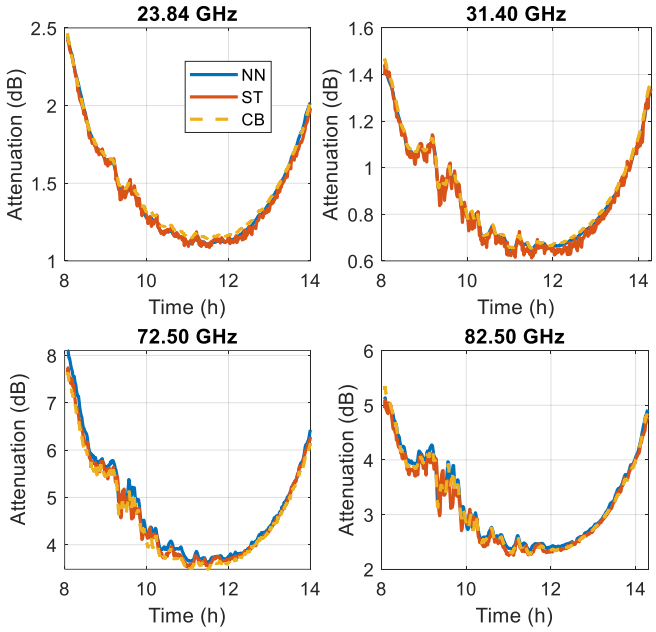

Fig. 7. Trend of the tropospheric attenuation on 28 November 2020 (clear sky), as estimated using the ST technique (red curve), the CB technique (yellow curve) and the neural network approach (blue curve).

A more complete assessment of the prediction accuracy can be obtained by evaluating the root mean square (RMS) value of the absolute prediction error ε, defined as:

$$\varepsilon(t) = A_{CB/ANN}(t) - A_{ST}(t) \ \text{(dB)} \qquad (10)$$

where $A_{CB/ANN}(t)$ is the attenuation estimated using either the CB technique or the ANN approach, for every sample in a day, while $A_{ST}(t)$ is the ST-based attenuation.

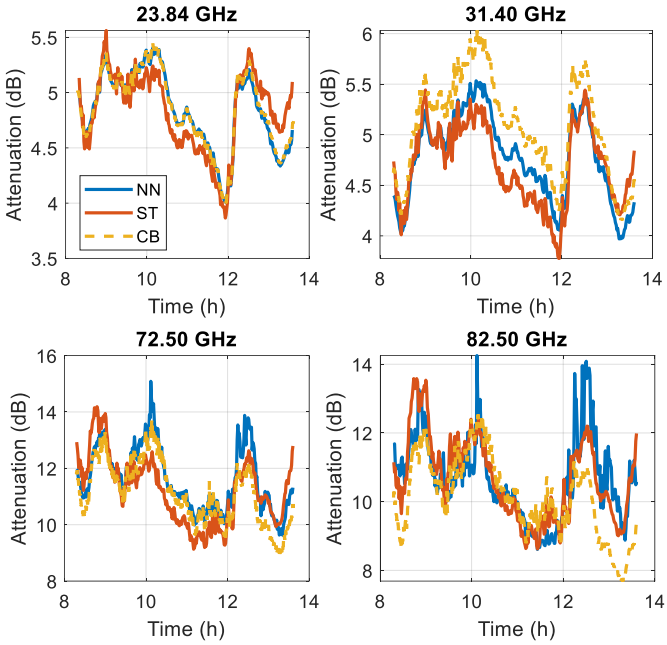

Fig. 8. Trend of the tropospheric attenuation on the 8 December 2020 (light rain), as estimated using the ST technique (red curve), the CB technique (yellow curve) and the neural network approach (blue curve).

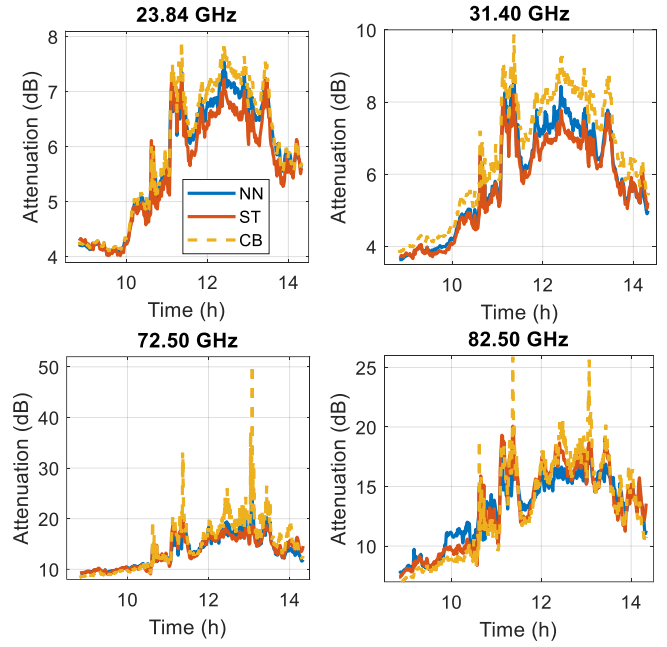

Fig. 9. Trend of the tropospheric attenuation on the 2 January 2021 (moderate rain), as estimated using the ST technique (red curve), the CB technique (yellow curve) and the neural network approach (blue curve).

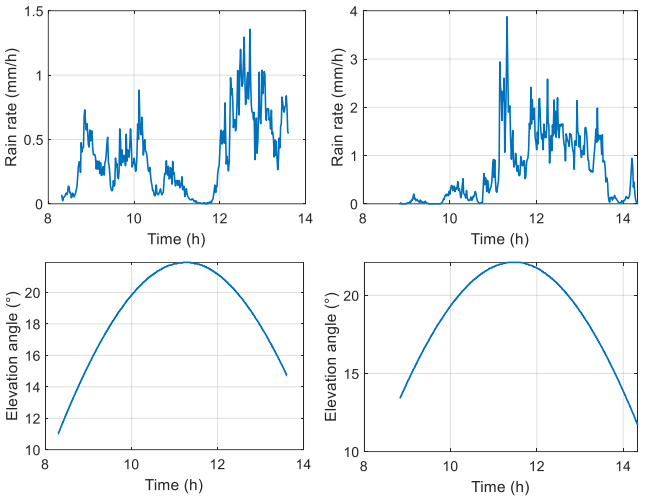

Fig. 10. Rain intensity trend and Sun elevation angles for 8 December 2020 (left side) and 2 January 2021 (right side).

Fig. 11 and Fig. 12 depict the daily RMS value, calculated by considering separately the rain free days and the rainy ones, respectively. The former figure clearly indicates that the prediction performance of the two methods is quite high and fully comparable. In both cases, the RMS value never exceeds 0.8 dB both at Ka band and W band, respectively. The peak error in Fig. 11 at Ka band (≈ 0.5 dB at 23.84 GHz and ≈ 0.7 dB at 31.40 GHz) is associated to the overestimation of the attenuation using the ST method at the beginning of the day (elevation angle around 10°), in turn likely due to an obstacle partially obstructing the path to the Sun (e.g. construction crane). As for rainy days, the results shown in Fig. 12 corroborate the findings reported in Fig. 8 and Fig. 9: while the RMS associated to the ANN approach falls approximately below 2 dB and 2.5 dB at Ka band and W band, respectively, the one obtained from the CB technique reaches peaks of roughly 4.5 dB and 5 dB at Ka band and W band, respectively.

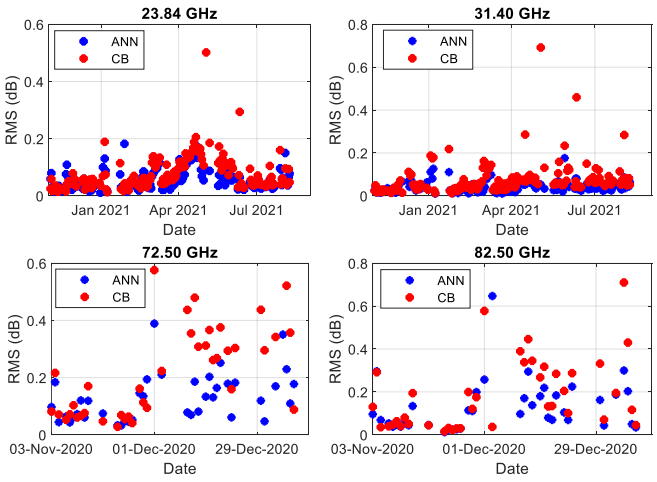

Fig. 11. RMS of the prediction error using the ANN approach (blue dots) and the CB technique (red dots): rain free days (test plus training/validation datasets).

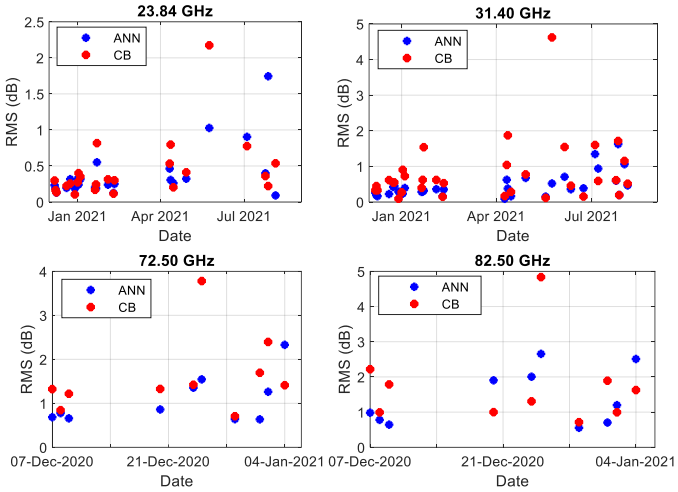

Fig. 12. RMS of the prediction error using the ANN approach (blue dots) and the CB technique (red dots): rainy days (test plus training/validation datasets).

For the sake of completeness, Fig. 13 shows the same information as in Fig. 11 and Fig. 12, but considering only the ANN test dataset (rain free plus rainy days).

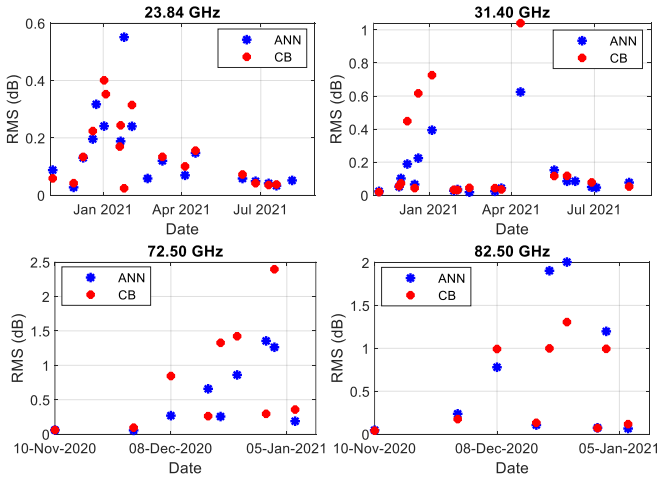

Fig. 13. RMS of the prediction error using the ANN approach (blue dots) and the CB technique (red dots): rain free plus rainy days (only test dataset).

B. *Statistical Analysis*

The statistical analysis of results is of key importance for system design purposes, more specifically to determine the atmospheric margin to be assigned to any Earth-space link.

Fig. 14 and Fig. 15 depict the Complementary Cumulative Distribution Functions (CCDFs) of the A_{ST}, A_{CB} and A_{NN}, at 31.40 and 82.50 GHz respectively, for all the rain-free samples. As already pointed out in Section V.A, a very good agreement emerges at 31.40 GHz by comparing the different curves, while a slightly higher discrepancy is visible at 82.50 GHz, up to 1 dB for the exceedance probability P ranging roughly from 0.005 and 0.05.

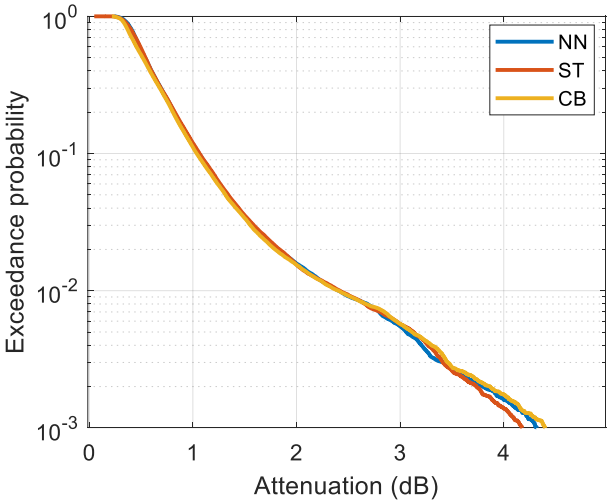

Fig. 14. CCDF of the tropospheric attenuation at 31.40 GHz under rain-free conditions.

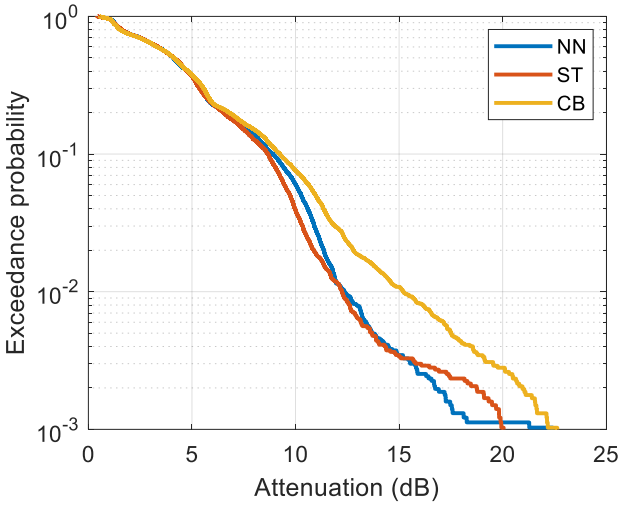

Fig. 16. CCDF of the tropospheric attenuation at 23.84 GHz under rainy conditions.

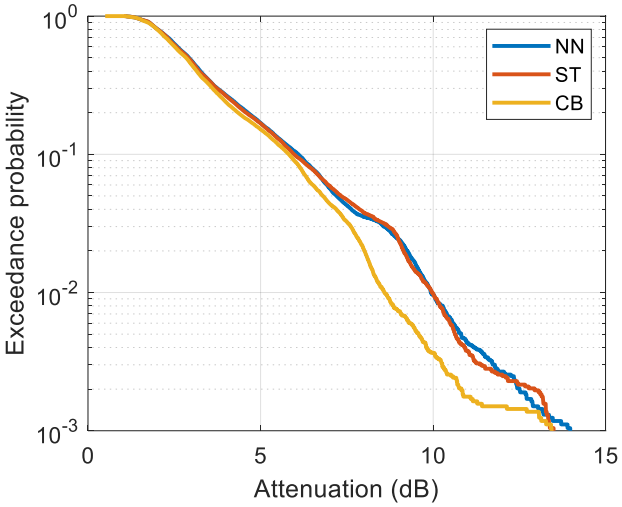

Fig. 15. CCDF of the tropospheric attenuation at 82.50 GHz under rain-free conditions.

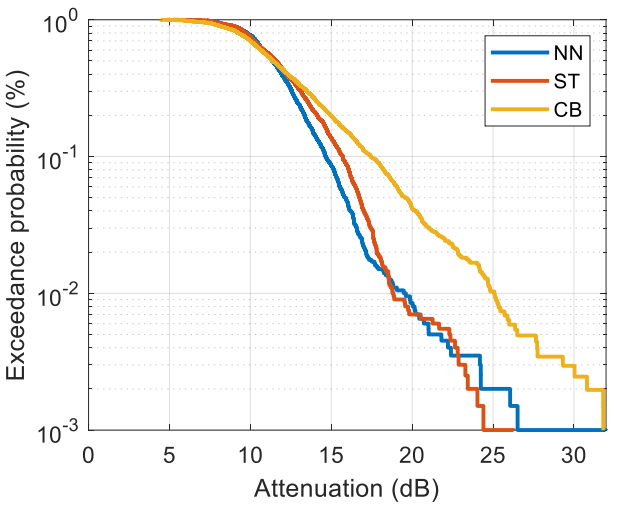

Fig. 17. CCDF of the tropospheric attenuation at 72.50 GHz under rainy conditions.

As expected, a much larger difference between the different approaches appears in Fig. 16 and Fig. 17, which show the CCDFs of the tropospheric attenuation at 23.84 and 72.50 GHz respectively, for all the rainy samples: the lower the probability value and the higher the frequency, the more marked is the overestimation of A_{CB} over A_{ST}, reaching approximately 15 dB for P = 0.001 and f = 72.5 GHz. On the contrary, the discrepancy between A_{NN} and A_{ST} is quite limited at both frequencies, thus indicating the ability of the neural network to provide accurate predictions of the tropospheric attenuation also under rainy conditions.

C. All-Weather Combined Prediction Model (AWCPM)

As discussed in Section II.A, the CB approach is a well-established technique allowing an accurate retrieval of the tropospheric attenuation in rain free situations [7]. Moreover, whenever physically-based closed-form inversions are available, they should be preferred over empirical or machine learning techniques, which obviously have a lower degree of global applicability. In this context, this section outlines a methodology to combine the advantages originating from the high accuracy of CB inversions in scattering free conditions with those coming from the proposed ANN under rainy conditions. The key prerequisite is the ability to spot the presence of precipitation along the path, which can be achieved by resorting to the Sky Status Indicator (SSI), defined as [32]:

$$\mathrm{SSI} = \frac{T_{A-oos}(31.40)-9.19}{T_{A-oos}(23.84)} \tag{11}$$

Setting different thresholds on the SSI allows having an estimate of the meteorological status along the path. Namely:

- SSI < 0.4: clear sky;
- 0.4 ≤ SSI < 0.87: cloudy conditions;
- SSI ≥ 0.87: rainy sky conditions.

Therefore, taking advantage of the SSI, the following All-Weather Combined Prediction Model (AWCPM) is devised:

1. for each instant, calculate the SSI from T_{A-oos} at 23.84 and 31.40 GHz;
2. if SSI < 0.87 (scattering free conditions), apply (4) to obtain *A*;
3. if SSI ≥ 0.87 (scattering conditions), apply the proposed ANN to derive *A*.

It is worth mentioning that the SSI is a statistical tool: 0.87 is a sort of average threshold maximizing the accuracy in identifying the presence of precipitation along the path [32]. The misidentification of meteorological conditions will typically occur for the heavy cloud/light rain cases, neither of which is critical for the retrieval method accuracy. In fact, when SSI ≥ 0.87 but no rain is actually present along the path, the ANN has proven to be accurate. On the other hand, if SSI < 0.87, but some light rain is actually present, the CB approach is still expected to provide accurate results, as the amount of scattering is quite limited. This is proven by the results reported in Fig. 18 and Fig. 19 at 23.84 and 72.50 GHz, respectively: the agreement between the retrievals obtained using the AWCPM and the ST technique, used as reference, is very good for all exceedance probability values. Comparable results, not included for the sake of brevity, are obtained at 31.40 and 82.50 GHz.

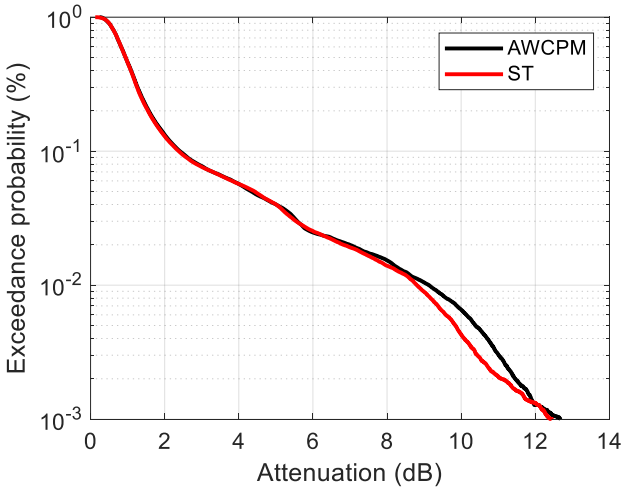

Fig. 18. CCDF of the tropospheric attenuation at 23.84 GHz: comparison between the application of the AWCPM and the ST technique.

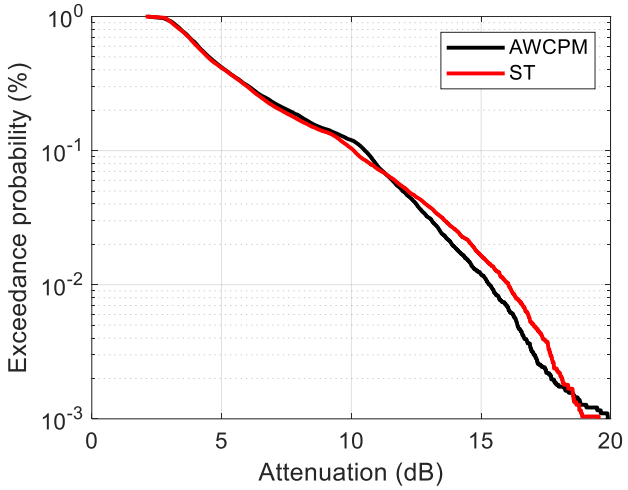

Fig. 19. CCDF of the tropospheric attenuation at 72.50 GHz: comparison between the application of the AWCPM and the ST technique.

VI. Conclusions

This work proposed a novel mixed physically-based/machine learning approach to measure tropospheric attenuation *A* affecting Earth-space links in all-weather conditions. The measurement technique relies on the use of microwave radiometers, and, as such, it offers a valid less expensive alternative to carrying out typical propagation experiments which exploit space-borne beacon signals. This is even more so at W band, for which no long-term measurements nor space-borne signals (from GEO satellites) currently exist. Moreover, the proposed approach combines the advantages originating from the accurate *A* retrievals provided by the well-established Cosmic Background approach in clear-sky conditions with the benefits coming from machine learning techniques, which can offer a simplified solution for the estimation of *A* in rainy conditions, if compared to the application of the Radiative Transfer Equation and/or the Sun-Tracking technique.

Four artificial neural networks were devised to convert the antenna noise temperature T_A measured by a 4-channel Ka-band/W-band MWR into mean radiating temperature T_{mr} at 23.8 GHz, 31.4 GHz, 72.5 GHz and 82.5 GHz, from which *A* can be easily derived. The networks, which also receive as input the local meteorological parameters, were properly trained and tested by taking advantage of the concurrent CB and ST measurements collected by the RpG radiometer deployed at Politecnico di Milano, Italy, under the ESA funded WRAD project. Tests have shown that, in scattering free conditions, the ANNs prediction accuracy is comparable to the one provided by the more customary CB technique (e.g. average RMS_{ANN} = 0.18 dB and RMS_{CB} = 0.23 dB), while in rainy conditions, the machine learning approach achieves a lower estimation error (e.g. average RMS_{ANN} = 1.39 dB and RMS_{CB} = 3.20 dB). Based on these results, and considering the sound physical basis of the well-established CB measurement technique, an All-Weather Combined Prediction Model was devised, which combines the benefits of the CB technique and of the ANN: taking advantage of the SSI to identify precipitation along the path, the former is applied in scattering free conditions, while the latter is

employed during rain events. Statistical results indicate that AWCPM offers a very accurate prediction of the CCDF of A both at Ka and W band, which, in turn, represents a key piece of information for the design of Earth-space links.

Starting from these encouraging but preliminary results, future work will include corroborating AWCPM by taking advantage of more extensive additional Ka-/W-band measurements collected in other sites (e.g. Rome, NY [12]): while the model's framework is expected to be applicable worldwide, the accuracy of the ANNs derived in this work for different measurement periods and in other sites might decrease. Additionally, the use of ANNs with memory layers (e.g. LSTM − Long Short-Term Memory) will be taken into account to further improve the accuracy of AWCPM.

APPENDIX

A new analytical model is proposed to estimate the mean radiating temperature, according to its dependence on the elevation angle (as pointed out, e.g., in [8]) and on the ground values of pressure (P_S), temperature (T_S) and relative humidity (RH_S) (whose correlation with T_{mr} is discussed in [12] and [26], for example). The model was devised by resorting to 10 years of radiosonde observation (RAOBS) collected twice a day (0 and 12 UTC) at Milano/Linate airport, lying at 5 km of distance from the site where the MWR is installed. As summarized in Fig. 20, the model was developed using the vertical profiles of pressure (P), temperature (T) and relative humidity (RH) as input to the MPM93 mass absorption model proposed in [33] to calculate the mean radiating temperature $T_{mr}(f,\theta)$, for a given elevation angle θ and each of the four radiometric frequencies f. The analysis of the results pointed out that T_{mr} is linearly correlated to T_S and RH_S (as also discussed in [12]), and only weakly dependent on P_S, which was therefore neglected in the model development. Specifically, the following equation was used to relate the mean radiating temperature to the ground meteorological variables:

$$T_{mr}(f,\theta) = a_0(f,\theta) + a_1(f,\theta)T_S + a_2(f,\theta)RH_S \quad (12)$$

where the coefficients $a_j(f,\theta)$ (j = 0, 1, 2) were regressed from the calculated $T_{mr}(f,\theta)$ and the RAOBS first-level values of the temperature (T_S — in K) and relative humidity (RH_S — in %) profiles (see Fig. 20).

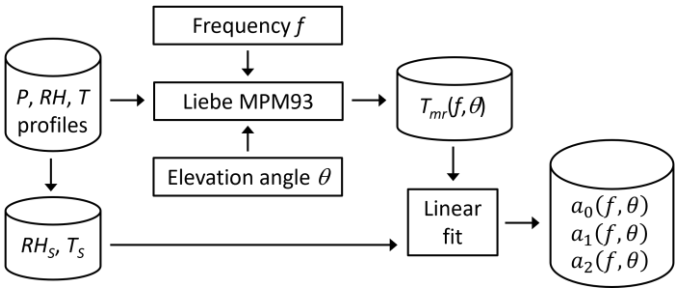

Fig. 20. Summary of the T_{mr} analytical model development process.

The process illustrated in Fig. 20 was repeated for different elevation angles, ranging from 10° to 90°. Finally, the following double exponential model for the coefficients a_0, a_1 and a_2 was derived:

$$a_j(f,\theta) = b_{0,j}(f)e^{b_{1,j}(f)\theta} + b_{2,j}(f)e^{b_{3,j}(f)\theta} \quad (13)$$

where j = 0, 1, 2 indicates the a coefficient number and θ is the elevation angle expressed in degrees. The coefficients $b_{k,j}$ (k = 0, 1, 2, 3 indicating the b coefficient number) are listed in Table V, Table VI, Table VII and Table VIII for 23.84, 31.4, 72.5 and 82.5 GHz, respectively.

As an example, Fig. 21 shows the trend of coefficient a_2 at f = 82.5 GHz, which is precisely fitted by the expression in (13). Similar results are obtained for a_0 and a_1.

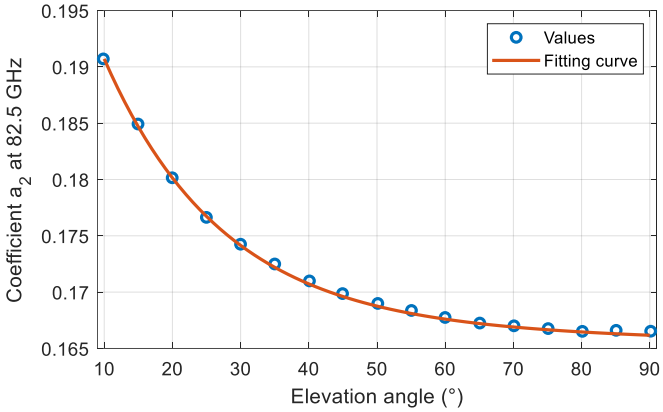

Fig. 21. Trend of coefficient a_2 in (12) at 82.5 GHz as a function of the elevation angle.

TABLE V. COEFFICIENTS b IN (13) FOR EACH COEFFICIENT a IN (12) AT f = 23.84 GHz.

	b_0	b_1	b_2	b_3
a_0	-53.1	-0.094	3.93	6.3×10^{-3}
a_1	0.193	-0.098	0.91	-1.65×10^{-4}
a_2	0.03	-0.089	0.138	-2.32×10^{-4}

TABLE VI. COEFFICIENTS b IN (13) FOR EACH COEFFICIENT a IN (12) AT f = 31.4 GHz.

	b_0	b_1	b_2	b_3
a_0	-26.2	-0.102	-16.2	-1.4×10^{-3}
a_1	0.098	-0.102	0.96	-7.7×10^{-5}
a_2	0.02	-0.091	0.166	-1.35×10^{-4}

TABLE VII. COEFFICIENTS b IN (13) FOR EACH COEFFICIENT a IN (12) AT f = 72.5 GHz.

	b_0	b_1	b_2	b_3
a_0	-42.4	-0.059	-16.6	-7.74×10^{-4}
a_1	0.19	-0.067	0.96	-1.08×10^{-4}
a_2	0.028	-0.026	0.165	3.32×10^{-4}

TABLE VIII. COEFFICIENTS b IN (13) FOR EACH COEFFICIENT a IN (12) AT f = 82.5 GHz.

	b_0	b_1	b_2	b_3
a_0	-63.3	-0.078	-22.07	-0.0026
a_1	0.24	-0.08	0.99	-1.84×10^{-4}
a_2	0.043	-0.057	0.167	-6.49×10^{-5}

Fig. 22 shows the trend of T_{mr} as a function of the elevation angle according to the model in (12), for T_S = 288 K and RH_S = 50%: the 10°-90° peak-to-peak variation of T_{mr} is approximately 2, 1.5, 7 and 4 K at 23.84, 31.4, 72.5 and 82.5 GHz, respectively.

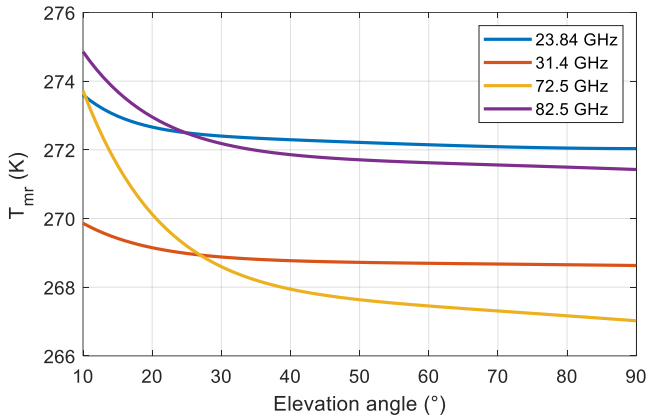

Fig. 22. Trend of T_{mr} as a function of the elevation angle according to the model in (12), for T_S = 288 K and RH_S = 50%.

Fig. 23 compares the mean radiating temperature as calculated from the RAOBS profiles (see Fig. 20) and as estimated using the analytical model in (12). Results refer to two full years of the available dataset at f = 82.5 GHz and θ = 45°.

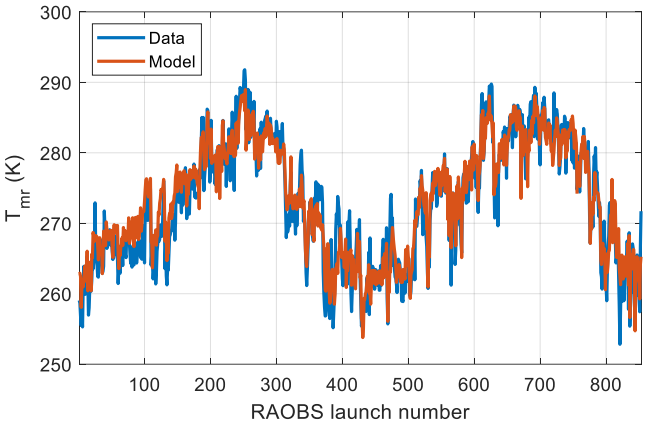

Fig. 23. Mean radiating temperature as calculated from the RAOBS profiles (see Fig. 20) and as estimated using the analytical model in (12); two full years of the available dataset, f = 82.5 GHz and θ = 45°.

The discrepancy between the curves in Fig. 23 can be quantified by using the error figure ε defined as:

$$\varepsilon(t,f,\theta) = T_{mr}^{E}(t,f,\theta) - T_{mr}^{M}(t,f,\theta) \text{ (K)} \quad (14)$$

where $T_{mr}^{E}(t,f,\theta)$ and $T_{mr}^{M}(t,f,\theta)$ are the mean radiating temperatures estimated using the model in (12) and calculated from the RAOBS measurements, respectively, and t represents the RAOBs launch number. Table IX and Table X offer a comprehensive description of the T_{mr} model performance by listing the mean value (E) and the root mean square (RMS) value of the error figure in (14), for each of the four radiometric frequencies and as a function of selected elevation angles. Results indicate quite a stable performance, with E ranging between -0.1 K and 1.9 K, and with RMS limited to 3.4 K.

TABLE IX. MEAN VALUE (K) OF THE ERROR FIGURE IN (14).

	10°	**20°**	**30°**	**40°**	**50°**	**60°**	**70°**	**80°**	**90°**
23.84 GHz	0.1	0.1	0.1	0.1	0.1	0.1	0.1	0.1	-0.1
31.4 GHz	1.2	1.2	1.1	1.1	1.1	1.1	1.1	1.1	1.1
72.5 GHz	1.9	1.6	1.3	1.2	1.2	1.2	1.2	1.1	1
82.5 GHz	1.4	1.2	0.9	0.9	0.9	0.9	0.9	0.9	0.8

TABLE X. ROOT MEAN SQUARE VALUE (K) OF THE ERROR FIGURE IN (14).

	10°	**20°**	**30°**	**40°**	**50°**	**60°**	**70°**	**80°**	**90°**
23.84 GHz	2.8	2.9	2.9	3	3	3	3	3	3
31.4 GHz	3.1	3.2	3.2	3.2	3.2	3.2	3.2	3.2	3.2
72.5 GHz	3.4	3.3	3.1	3.1	3.1	3.1	3.1	3.1	3
82.5 GHz	3.1	3.1	3.1	3.1	3.1	3.1	3.1	3.1	3.1

ACKNOWLEDGMENT

Acknowledgments go to: the European Space Agency (ESA) for partially supporting this activity under the ESTEC Contract 4000125141/18/NL/AF "WRAD - Characterization of W-band propagation channel through ground-based observations (Expro plus)", as well as all the colleagues involved in such project; the European Office of Aerospace Research and Development (EOARD) for partially supporting this activity under the EOARD award No. FA8655-22-1-7171 "MMWAP - MilliMeter Wave Atmospheric Propagation: advancing microphysical-radiative modeling, statistical characterization and neural-network prediction of cloud attenuation and emission"; NASA for making available the rain rate data within the collaboration with Politecnico di Milano on the Alphasat Aldo Paraboni propagation experiment; Simone Sipala for his help with the calculations on the data.

REFERENCES

[1] C. Riva, C. Capsoni, L. Luini, M. Luccini, R. Nebuloni and A. Martellucci, "The challenge of using the W band in satellite communication", Int. J. Satell. Commun. Network, vol. 32, pp. 187–200, 2014.

[2] J. E. Allnutt, "Satellite to ground radiowave propagation," the Institution of Engineering and Technology, 2nd edition, March 2011.

[3] F. Cuervo, A. M. Polegre, D. Vanhoenacker-Janvier, J. Flávio, M. Schmidt, "The Q/W-band CubeSat LEO Propagation Experiment," 2021 15th European Conference on Antennas and Propagation (EuCAP), Dusseldorf, Germany, 2021, pp. 1-5.

[4] Recommendation ITU-R P.618-13, "Propagation data and prediction methods required for the design of Earth-space telecommunication systems," Geneva, 2017.

[5] G. Codispoti, G. Parca, M. Ruggieri, T. Rossi, M. De Sanctis, C. Riva, L. Luini, "The Role of the Italian Space Agency in Investigating High Frequencies for Satellite Communications: the Alphasat Experiment", International Journal of Satellite Communications and Networking, Vol. 37, Issue 5, Special Issue: Alphasat Aldo Paraboni Ka and Q/V experiment, pp. 387-396, September/October 2019.

[6] F. Giannetti, M. Moretti, R. Reggiannini, A. Vaccaro, "The NEFOCAST system for detection and estimation of rainfall fields by the opportunistic use of broadcast satellite signals," IEEE Aerospace and Electronic Systems Mag., vol. 34, no. 6, pp. 16–27, Jun. 2019.

[7] L. Luini, C. Riva, C. Capsoni, and A. Martellucci. "Attenuation in nonrainy conditions at millimeter wavelengths: Assessment of a procedure," IEEE Transactions on Geoscience and Remote Sensing, 45(7):2150–2157, 2007.

[8] Y. Han, E. R. Westwater, "Analysis and improvement of tipping calibration for ground-based microwave radiometers," IEEE Transactions

on Geoscience and Remote Sensing, vol. 38, no. 3, pp. 1260-1276, May 2000.

[9] L. Luini, C. Riva, R. Nebuloni, M. Mauri, J. Nessel, A. Fanti, "Calibration and Use of Microwave Radiometers in Multiple-site EM Wave Propagation Experiments", EuCAP 2018, pp. 1-5, 9-13 April 2018, London, UK.

[10] L. Tsang, J. Kong, E. Njoku, D. Staelin, J. Waters, "Theory for microwave thermal emission from a layer of cloud or rain," IEEE Transactions on Antennas and Propagation, vol. 25, no. 5, pp. 650-657, September 1977.

[11] D. Long, F. Ulaby, "Microwave Radar and Radiometric Remote Sensing," Artech, 2015.

[12] F. S. Marzano, V. Mattioli, L. Milani, K. M. Magde, and G. A. Brost. "Sun-tracking microwave radiometry: All-weather estimation of atmospheric path attenuation at Ka -, V -, and W -band." IEEE Transactions on Antennas and Propagation, 64(11): 4815–4827, 2016.

[13] V. Mattioli, L. Milani, K. M. Magde, G. A. Brost, F. S. Marzano, "Retrieval of Sun Brightness Temperature and Precipitating Cloud Extinction Using Ground-Based Sun-Tracking Microwave Radiometry," IEEE Journal of Selected Topics in Applied Earth Observations and Remote Sensing, vol. 10, no. 7, pp. 3134-3147, July 2017.

[14] L. Luini, C. Riva, F. S. Marzano, M. Biscarini, L. Milani, D. Cimini, S. T. Nilo, A. Martellucci, "Development and Application of Advanced Experimental Techniques for Ground Microwave Radiometry in All Weather Conditions," EuCAP 2023, pp. 1-5, 26-31 March 2023, Florence, Italy.

[15] F. J. Tapiador, C. Kidd, K.-L. Hsu, F. Marzano, "Neural networks in satellite rainfall estimation," Royal Meteorological Society (RMetS), 2006.

[16] Tapiador, Francisco J., et al. "A Neural Networks–Based Fusion Technique to Estimate Half-Hourly Rainfall Estimates at 0.1° Resolution from Satellite Passive Microwave and Infrared Data." Journal of Applied Meteorology (1988-2005), vol. 43, no. 4, 2004, pp. 576–94.

[17] Rivolta, G., Marzano, F. S., Coppola, E., and Verdecchia, M.: Artificial neural-network technique for precipitation nowcasting from satellite imagery, Adv. Geosci., 7, 97–103, 2006.

[18] F. S. Marzano, E. Fionda, P. Ciotti, "Neural-network approach to ground-based passive microwave estimation of precipitation intensity and extinction," Journal of Hydrology, Volume 328, Issues 1–2, 2006, Pages 121-131.

[19] L. Wu et al., "Prediction of atmospheric noise temperature at the deep space network with machine learning," Radio Science, vol. 57, no. 11, pp. 1-11, Nov. 2022.

[20] M. Biscarini, G. Stazi, L. Milani, L. Luini, C. Riva, D. Cimini, S. T. Nilo, S. Gentile, F. Romano, G. Brost, A. Martellucci, "Statistical Modeling of Atmospheric Propagation Channel at W-Band Through Sun-Tracking Microwave Radiometric Measurements for Non-Geostationary Satellite Links," in IEEE Transactions on Antennas and Propagation, vol. 71, no. 9, pp. 7512-7522, Sept. 2023.

[21] F. T. Ulaby, R. K. Moore, A. K. Fung, "Microwave Remote Sensing", Addison-Wesley, Reading 1981.

[22] R.M. Allnutt, T. Pratt, W.L. Stutzman, and J.B. Snider, "Use of radiometers in atmospheric attenuation measurments", IEE Proc. Microw. Antennas Propag. Vol 141, 428-432, 1994.

[23] M. Biscarini, F. S. Marzano, "Generalized Parametric Prediction Model of the Mean Radiative Temperature for Microwave Slant Paths in All-Weather Condition," IEEE Transactions on Antennas and Propagation, vol. 68, no. 2, pp. 1031-1043, Feb. 2020.

[24] S. I. Karhu, P. Jokela, E. T. Salonen, "Atmospheric attenuation statistics of 11 years measured by a 12 GHz radiometer in Finland," Proceedings of the 21st European Microwave Conference, Stuttgart, Germany, 9-12 September 1991, Vol. 2, pp. 1229-1234.

[25] R.R. Bell, "Calibration of 20 and 30 GHz radiometers by using the ATS–6 satellite beacons," Electronics Letters, vol 13, pp 412-413, 1977.

[26] G. Brost, K. Magde, "On the use of the radiometer formula for atmospheric attenuation measurements at GHz frequencies," 2016 10th European Conference on Antennas and Propagation (EuCAP), 2016, pp. 1-5.

[27] G. Karatas, "The Effects of Normalization and Standardization an Internet of Things Attack Detection," European Journal of Science and Technology Special Issue 29, pp. 187-192, December 2021.

[28] N. M. Nawi, W. H. Atomi, M. Z. Rehman, "The Effect of Data Pre-Processing on Optimized Training of Artificial Neural Networks," The 4th International Conference of Electrical Engineering and Informatics (ICEEI 2013), pp. 1-8, Procedia Technology 11 (2013) 32 – 39.

[29] T. Zhan, M. Gong, X. Jiang, S. Li, "Log-Based Transformation Feature Learning for Change Detection in Heterogeneous Images," IEEE Geoscience and Remote Sensing Letters, Vol. 15, No. 9, September 2018.

[30] E. Alpaydin, "Introduction to machine learning", Fourth Edition, Cambridge, Massachusetts: The MIT Press, 2020.

[31] MathWorks. fitrnet - train neural network regression model, 2021. URL "https: //ch.mathworks.com/help/stats/fitrnet.html."

[32] A. V. Bosisio, E. Fionda, P. Ciotti, and A. Martellucci, "A sky status indicator to detect rain-affected atmospheric thermal emissions observed at ground," IEEE Transactions on Geoscience and Remote Sensing, 51(9):4643–4649, 2013.

[33] H. J. Liebe, G. A. Hufford, M. G. Cotton, "Propagation modelling of moist air and suspended water/ice particles at frequencies below 1000 GHz," AGARD 52nd Specialists' Meeting of The EM Wave Propagation Panel, Palma De Maiorca, Spain, 1993.